Heliyon

Received:
1 February 2017
Revised:
18 May 2017
Accepted:
23 June 2017

Cite as: Jeff M. Byers, Joseph A. Christodoulides, James B. Delehanty, Deepa Raghu, Marc P. Raphael . Quantifying time-varying cellular secretions with local linear models. Heliyon 3 (2017) e00340. doi: 10.1016/j.heliyon.2017.e00340

Quantifying time-varying cellular secretions with local linear models

Jeff M. Byers, Joseph A. Christodoulides, James B. Delehanty, Deepa Raghu, Marc P. Raphael *

Naval Research Laboratory, 4555 Overlook Ave SW, Washington, DC 20375-5320

* Corresponding author.

E-mail address: marc.raphael@nrl.navy.mil (M.P. Raphael).

Abstract

Extracellular protein concentrations and gradients initiate a wide range of cellular responses, such as cell motility, growth, proliferation and death. Understanding inter-cellular communication requires spatio-temporal knowledge of these secreted factors and their causal relationship with cell phenotype. Techniques which can detect cellular secretions in real time are becoming more common but generalizable data analysis methodologies which can quantify concentration from these measurements are still lacking. Here we introduce a probabilistic approach in which local-linear models and the law of mass action are applied to obtain time-varying secreted concentrations from affinity-based biosensor data. We first highlight the general features of this approach using simulated data which contains both static and time-varying concentration profiles. Next we apply the technique to determine concentration of secreted antibodies from 9E10 hybridoma cells as detected using nanoplasmonic biosensors. A broad range of time-dependent concentrations was observed: from steady-state secretions of 230 pM near the cell surface to large transients which reached as high as 56 nM over several minutes and then dissipated.

Keywords: Biophysics, Biotechnology, Cell biology, Mathematical bioscience, Nanotechnology

http://dx.doi.org/10.1016/j.heliyon.2017.e00340

1. Introduction

From bacterium to eukaryote, a cell's fate is directly tied to its local chemical environment. The measurement of external protein concentrations and gradients by membrane bound receptors has been found to determine the most fundamental of cellular decisions including differentiation (Letterio and Roberts, 1998; Risau and Flamme, 1995), motility (Friedl and Gilmour, 2009; Heldin and Westermark, 1999; Werner and Grose, 2003), growth (Conlon et al., 2001; Raff et al., 1978), proliferation (Beck and Damore, 1997; Hogan, 1996) and death (Ashkenazi and Dixit, 1998; Hershko and Ciechanover, 1998; Nagata, 1997). For decades such dependencies have been deduced by introducing artificial gradients of signaling molecules to cell cultures either on the surface (Brandley and Schnaar, 1989; Dertinger et al., 2002; Whitesides et al., 2001) or more recently in solution using microfluidic-based instrumentation (El-Ali et al., 2006; Jeon et al., 2002; Lucchetta et al., 2005; Yang et al., 2002). The resulting concentration profiles can be well-defined by the experimental geometry, flow rates and diffusion constants, giving quantitative insights into the relationship between the distribution of signaling molecules and cellular response. Unfortunately such designs are a poor approximation for the complex gradients produced by cells either in culture or *in vivo*. Furthermore, such artificial gradients cannot probe the intrinsic interplay of the intercellular communication system in which cells act as both the local signaling sources and receivers. To understand cellular behavior in environments that more closely mimic *in vivo* conditions there is a need to quantify the time-dependent protein concentrations as secreted by the cells themselves. Such measurements can then be utilized by mechanistic models of cell behavior which require such quantitative data sets for testing predictions. (Licko, 1973; Sunnaker et al., 2013; Tsaneva-Atanasova et al., 2010)

There now exists a number of sensing techniques capable of detecting time-dependent secretions from individual or groups of cells using either fluorescent (Han et al., 2010; Shirasaki et al., 2014) or nanoplasmonic sensors (Raphael et al., 2013a) as the signal transduction mechanism. These sensors give a response which is functionally related to the number of analyte molecules captured on the sensor surface but do not directly measure analyte concentration in solution. The challenge, then, is to infer the time-dependent concentration of cell secretions in solution, C, from the affinity-based binding measurements at the sensor surface. The relationship between these two quantities is governed by the law of mass action (Eq. (1))

$$\dot{f} = k_a C \cdot (1 - f) - k_d f \tag{1}$$

which is written in terms of the fractional occupancy of surface bound receptors, f, and its time derivative, $\dot{f}$ (k_a is the association rate constant and k_d is the dissociation rate constant). If cellular secretions reach a steady state then $\dot{f}$ is zero

http://dx.doi.org/10.1016/j.heliyon.2017.e00340

and the equation simplifies to a relation in which C is only functionally dependent on f. More generally, however, in processes involving cell proliferation (i.e development, cancer metastasis) or damage (i.e. wound healing, regeneration) the concentration profiles are far from steady state and the fractional occupancy's time derivative must be taken into account. For such cases a generalizable data analysis approach capable of determining temporal fluctuations in extra-cellular protein concentrations is required.

In this work we show such information can be obtained by the application of local linear models and temporal filtering of time-dependent fractional occupancy data. Using these approaches a joint probability distribution for f and $\dot{f}$ is determined and subsequently the concentration, C, with its associated error bars. We first illustrate the features and flexibility of this approach using simulated time-dependent concentration data. Next, we applied this approach to the analysis of antibody secretions from individual or small groups of hybridoma cells as measured with nanoplasmonic biosensors. The choice of the hybridoma as a model system was made for the following reasons: (1) these cell lines are engineered for constitutive antibody secretion, eliminating the added complexity of designing a secretion trigger (2) the optimal culturing conditions for hybridomas have been established over decades as have the bulk effects of perturbing these conditions by a variety of chemical and atmospheric conditions and (3) characterizing and optimizing the secretion rate of hybridomas (as well as CHO cells) is of central importance for producing research antibodies as well as the emergent class of immunotherapeutic drugs. Here we demonstrate that our data analysis method has the dynamic range to quantify concentrations from both steady-state and transient secretions on the 9E10 hybridoma cell line.

2. Materials and methods

2.1. Data simulations and analysis

All simulations and analysis were conducted using the Matlab 2013b environment with Curve Fitting, Image Processing and Statistics Toolboxes. Detailed derivations of the equations in the main text and their implementation in Matlab are described in the Supplementary Data.

2.2. Fabrication of nanostructure arrays

Square arrays of gold nanostructures were patterned using electron-beam nanolithography as previously described (Raphael et al., 2012). In short, the arrays were patterned onto No. 1.5 glass coverslips by spinning a bilayer resist structure consisting of polymethyl methacrylate and ethyl lactate methyl methacrylate copolymer with thicknesses of 180 nm and 250 nm, respectively. The resist was electron-beam patterned using doses 300 $\mu C/cm^2$ and subsequently

http://dx.doi.org/10.1016/j.heliyon.2017.e00340

developed for one minute in a 2:1 solution of isopropyl alcohol: methyl isobutyl ketone. A 5 nm layer of Ti followed by 80 ± 2 nm of Au was deposited with a Temescal electron-beam evaporator. The bilayer resist was then lifted off by soaking in acetone for 4 h. The bases of the nanostructures were circular in cross section with diameters of 75 ± 5 nm.

2.3. Nanostructure functionalization

RF plasma ashing (40 W) with 300 mTorr of a 5% hydrogen, 95% argon mixture was used to clean the glass and gold surfaces on the chips. The gold nanostructures were functionalized in a two-component ethanolic-based thiol bath (0.5 mM), consisting of a 3:1 ratio of SH-$(CH_2)_8$-EG_3-OH to SH-$(CH_2)_{11}$-EG_3-NH_2 (Prochimia) for 18 h, where EG stands for ethylene glycol monomer. The amine terminus was reacted with a 10 mg/mL solution of the heterobifunctional crosslinker sulfo-N-succinimidyl-4-formylbenzamide (Solulink) in PBS buffer at pH 7.4, followed by a hydrazine functionalized c-myc peptide conjugation (Solulink) in PBS buffer at pH 6.0 according to the manufacturer's instructions. In past work, anti-c-myc which had been exposed to a c-myc solution for blocking the binding antibody's binding sites gave a signal of 1% or less compared to its corresponding control study, demonstrating minimal non-specific binding to these surfaces (Raphael et al., 2013b). For biotin-neutravidin studies, 0.3 mM of sulfo-NHS-biotin (Thermo) in PBS was drop coated on to the chip for 30 min. Chips were rinsed with DDW and dried with nitrogen gas. Commercially available monoclonal anti-c-myc antibodies (Sigma) were used for normalizing array response at the end of each experiment.

2.4. Microscopy setup and drift correction

Halogen lamp light was first passed through a 594 long-pass filter and then the Koehler illumination train of an inverted microscope (Zeiss AxioObserver) before following the light path described in Fig. 1a. The objective used was a 63X, 1.46 numerical aperture oil-immersion objective. For spectral measurements a 600 μm diameter optical fiber was used to collect the scattered light from a single array and detected with thermoelectrically-cooled, CCD-based spectrophotometer (Ocean Optics QE65000) at an integration time of 1 s. A thermoelectrically-cooled CCD camera (Hamamatsu ORCA R2) with integration times between 200 and 250 ms was used for imagery. A heated stage and temperature controlled enclosure kept the stage temperature at 37.0 ± 0.04 °C (Zeiss). Humidity and CO_2 were regulated at 98% and 5%, respectively, by flowing a gas-air mixture though a heated water bottle and into the enclosure. In plane drift was corrected for with image alignment software (Zeiss Axiovision) while the focus was stabilized using an integrated hardware focus correction device (Zeiss Definite Focus).

http://dx.doi.org/10.1016/j.heliyon.2017.e00340

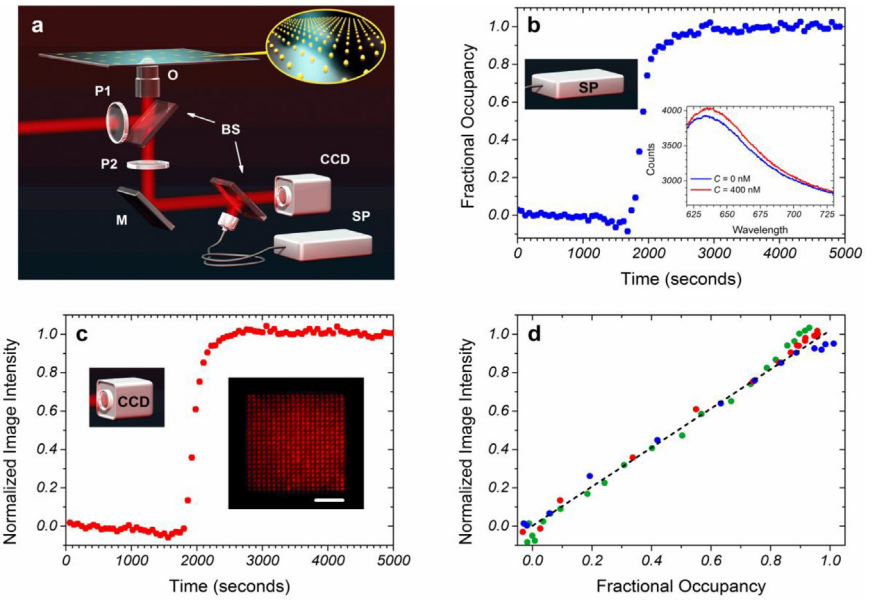

Fig. 1. LSPRi calibration using a 400 nanostructure array. (a) Gold nanostructures are patterned atop the coverslip (inset). The excitation light from a halogen lamp passes through a linear polarizer P1 and illuminates the arrays through the objective O. The reflected light is collected by the objective, passes through a crossed linear polarizer (P2) and is reflected by a mirror (M) through a 50/50 beam splitter (BS) to the spectrometer (SP) and CCD camera. (b) A single array is aligned with the fiber optic and the spectra is analyzed to determine the time-dependent fractional occupancy. The inset shows two spectra at concentrations $C = 0$ and $C = 400$ nM. (c) Normalized imagery data on the same array taken in parallel with the spectral acquisition. The inset shows a false colored CCD image of a 20×20 array of nanostructures with a pitch of 500 nm (scale bar is 3 μm). (d) Normalized image intensity versus the spectrally-determined fractional occupancy for three separate experiments. The red and green circles are for anti-c-myc monoclonal antibodies binding to a c-myc functionalized array in PBS and serum-free media, respectively. The blue circles are for neutravidin binding to biotinylated nanostructures. The size of the symbols in all plots incorporate 2σ uncertainty.

2.5. Hybridoma culturing

Clone 9E10 Hybridoma cells (ATCC) were cultured in complete growth medium RPMI-1640 supplemented with 10% fetal bovine serum and 1% antibiotic/antimycotic in a humidified tissue culture incubator at 37 °C under 5% CO2 atmosphere. Cells were maintained at a density of 3–5 $\times$ 10^5 cells/mL by performing passaging every two days which maintained viability at 90–95%. Prior to LSPRi studies, the cells were pelleted by centrifugation (900 rcf $\times$ 5 min) and washed twice with RPMI-1640 serum-free media (SFM) for the removal of secreted antibodies and serum. For imaging, 75 μL of 0.5–2 $\times$ 10^6 cells/mL cell solution was manually injected into the fluidics chamber. Cell surface density was controlled by allowing cells to settle on the surface for 5 to 10 min and then microfluidically flowing SFM to remove those still in solution.

http://dx.doi.org/10.1016/j.heliyon.2017.e00340

3. Results and discussion

3.1. Determining concentration from fractional occupancy

The initial data processing of the typical instrument for quantifying protein secretions produces an estimated fractional occupancy, f_i, and standard deviation, σ_i, for each of the M images at times t_i (Fig. 2a). Eq. (1), however, shows that the concentration is also dependent on the time derivative of the fractional occupancy, $\dot{f}$. A central problem for any data analysis approach that seeks to calculate time-varying concentration is that both f and $\dot{f}$, along with their related uncertainties, must first be jointly determined. The formalism we used to accomplish this can be thought of as divided into three steps. First, a time window, h, is defined in which f and $\dot{f}$ are to be calculated, as schematically shown in Fig. 2a. Second, the data within this time window are fit with a set of local linear models dependent on f and $\dot{f}$ (Fig. 2b) and a least-squares approach is used to determine their maximum likelihood values and uncertainties. Finally, the calculated joint probability

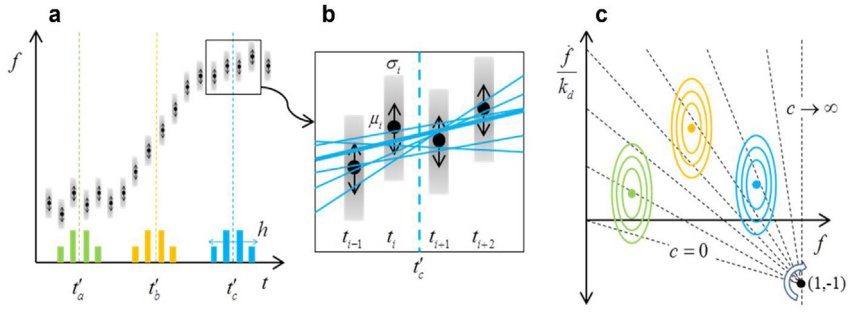

Fig. 2. Schematic of Data Analysis to Determine Concentration from Fractional Occupancy. Three steps are needed to determine the probability of a concentration at each time, t': (1) Subsampling the fractional occupancy, (2) forming the probability over parameters of local linear models and (3) integrating along lines of constant concentration. (a) The first step subsamples the processed LSPRi data, D, of mean values, μ_i (black circles) and standard deviations, σ_i (grey bars). A temporal filter centered at time, t, and width, h, assigns weights, w_i (depicted as vertical bars on the t-axis), to control the i^{th} sample's contribution to the local linear models. Three different times (t'_1, t'_2, and t'_3) are shown for determination of concentration. (b) A blow-up of the samples around $t = t'_3$ shows local linear models that might fit the data. Given the normal distribution (μ_i, σ_i) for the fractional occupancy at each ti one can quantify the probability of different local linear models explaining the data. The weights, w_i, subsample the data by increasing the variance of data outside the range of h via Eq. (4). Samples not near t'_3 are unable to constrain the linear models and do not contribute. (c) Each local linear model is a point in the $f - \dot{f}$ plane. All possible local linear models are summarized by the probability distribution, $p(f, \dot{f}|t, h; D)$, a bivariate normal distribution (depicted as elliptical contours) with five parameters: the mean value $(\bar{f}, \bar{\dot{f}})$ and the entries (σ_{xx}, σ_{xy}, and σ_{yy}) in the 2 × 2 covariance matrix, Σ. Using the law of mass action for the kinetic binding model, we can assign a concentration to each point $(f, \dot{f})$. The probability of a particular concentration, c, at a time t is determined by integrating $p(f, \dot{f}|t, h; D)$ along the lines of constant concentration shown as the dashed lines radiating from the point (1,-1). The constant value for the concentration of each line increases in the clockwise direction and each line integral must be successively evaluated to determine p(c|t, h; D) for all c.

http://dx.doi.org/10.1016/j.heliyon.2017.e00340

distribution for f and $\dot{f}$ is combined with Eq. (1) to determine the associated concentration probability distribution for each time window (Fig. 2c).

In describing the details of this approach some changes in nomenclature are helpful. First, substitute $f_i \rightarrow \mu_i$ to emphasize the connection with the mean parameter of the normal distribution. The processed data will then be indicated by $D = \{t_i, \mu_i, \sigma_i | i = 1, \ldots, M\}$. Also, define a dimensionless concentration: $c = C/K_D$. To summarize the procedure consider the following expression for the probability distribution of the concentration at time, t, conditioned on the data, D, and time window, h:

$$p(c|t,h;D) = \frac{1}{Z}\int_0^1 df \int_{-\infty}^{\infty} d\dot{f}\, p(c|f,\dot{f}) p(f,\dot{f}|t,h;D) \tag{2}$$

The parameter h determines the amount of data to subsample in D near the time, t, and the normalization, Z, is the integral of Eq. (2) over concentration:

$$Z(t,h;D) \equiv \int_0^{\infty} dc\, p(c|t,h;D) \tag{3}$$

The procedure is essentially error propagation of the uncertainty in μ_i as represented by σ_i via marginalization (*i.e.*, integrating over the model parameters f and $\dot{f}$, described below) to determine the probability distribution of the concentration, c, at each time, t, of interest, assuming a particular kinetic binding model represented by $p(c|f,\dot{f})$.

The calculation of $p(c|t,\ h\ ;\ D)$ is dependent upon $p(c|f,\dot{f})$ which is described by the kinetics of the reaction (Eq. (1)) and $p(f,\dot{f}|t,h;D)$ which, as discussed above, is a central computational challenge given that $\dot{f}$ is not explicitly measured. To determine $\dot{f}$, at a minimum we need to take a numerical derivative without amplifying the noise in the data. Standard practice in time-series analysis uses a smoothing filter over some range of samples in time, reducing the noise in the derivative. However, a better approach is possible in our experiment since we also have a standard deviation, σ_i, for each μ_i. This allowed us to pose the question, how well can a straight line, $\mu' = f + \dot{f}\cdot(t' - t)$, explain the noisy data near time t? Each local linear model with parameters $(f,\dot{f})$ over a range of data prescribed by the filter located at t with width, h, can be assigned a likelihood of fitting the data.

Similar to linear regression, we can write our probability as a negative log-likelihood, L, but with the weights, $w(t_i|t,\ h)$, of a temporal filter at each t_i of the data,

$$\begin{aligned} L &= -\ln p(f,\dot{f}|t,h;D) \\ &= \sum_{i=1}^{n} w(t_i|t,h)\cdot\frac{[f + \dot{f}\cdot(t_i - t) - \mu_i]^2}{2\sigma_i^2} + \text{terms ind. of } f \text{ and } \dot{f} \end{aligned} \tag{4}$$

Notice that the weights are effectively changing the variance of each sample in the local linear model. As $w_i \rightarrow 0$ for a sample, that sample acquires a large variance

http://dx.doi.org/10.1016/j.heliyon.2017.e00340

and does not constrain the choice of parameters for the linear models formed at t. If we used the maximum likelihood estimate of f and $\dot{f}$ at each time t then this technique is identical to re-weighted least squares. However, this point estimate only has value if we can also quantify its uncertainty and this necessitates a more detailed probabilistic model. Various functions can be selected for the temporal filter and we use a generic Gaussian profile, schematically shown as bar graphs in Fig. 2a, over the data acquisition times, $w(t_i|t,h) = e^{-(t_i-t)^2/2h^2}$, with two adjustable parameters: the center at time t and the width h. A different symmetric, location-scale function (e.g., Lorentzian, Epanechnikov) can be chosen as the filter with little change in the results. The only constraints are that the function needs to be positive and have a maximum value of one. A schematic drawing of linear fits to the data within a chosen filter time window is shown in Fig. 2b. (A discussion of the bias-variance tradeoff regarding the choice of h as well as the acausal nature of this filtering approach can be found in the Supplementary Data, Figs. S2 and S3).

Eq. (4) can be re-written as a bivariate normal distribution function, $p(f,\dot{f}|t,h;D)$ in terms of five parameters: the mean value $(\bar{f},\bar{\dot{f}})$ and the entries (σ_{xx}, σ_{xy}, and σ_{yy}) in the 2 × 2 covariance matrix, Σ. The probability distribution at each time point can be depicted as elliptical contours in $f-\dot{f}$ plane as shown in Fig. 2c and further detailed in the Supplementary Data, Fig. S1. When inserted into Eq. (2) the result is an integral that can be numerically evaluated at each time t over a range of concentrations to estimate the most probable concentration and its associated error (Supplementary Data).

3.2. Simulated measurements

To highlight the general features of the data analysis methodology described above we have simulated concentration data with varying time dependencies. Fig. 3a shows step-wise simulated $C(t)$ data in which the concentration increases slowly, then rapidly, and finally decreases rapidly. For the analysis we use k_a = 106 $M^{-1}s^{-1}$ and k_d = *10−3* s^{-1} which are values typical of antibody-antigen interactions.

The fractional occupancy versus time (Fig. 3b) is determined by numerically integrating the differential equation in Eq. (1) forward in time using the initial condition, $f(0) = 0$. Gaussian noise is added to the calculated $f(t)$ using a standard deviation typical of the experimental data shown in Fig. 1b. In Fig. 3c, the local linear models (red lines) are displayed for a Gaussian filter with h = 270 s and the resulting calculated concentration in Fig. 3d. Because of the relatively high association rate of the receptor-ligand pair, the slow and rapid concentration increases are faithfully reproduced by the analysis with some curvature at the vertices due to the filter width, h. The decreasing concentration step is reproduced but with a time delay of ~250 s due to the relatively long receptor-ligand mean

http://dx.doi.org/10.1016/j.heliyon.2017.e00340

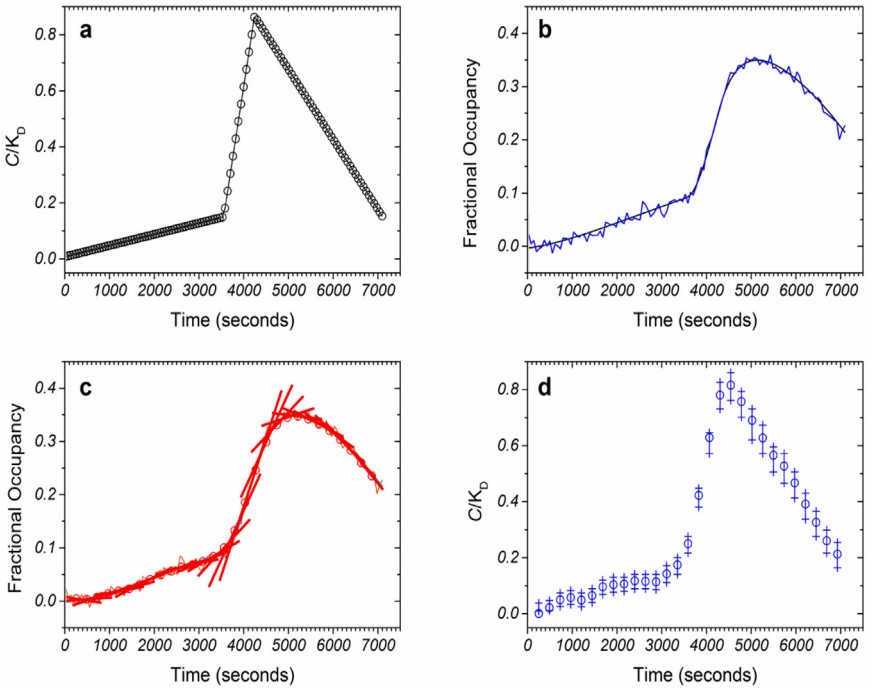

Fig. 3. Analysis of simulated concentration data for a receptor-ligand rate constants of k_a = 106 $M^{-1}s^{-1}$, k_d = 10−3 s^{-1}, K_D = 1 nM (a) Piece-wise function of three simulated time-dependent concentration scenarios (b) Time-dependent fractional occupancy as determined by solving Eq. (1) with added Gaussian noise typical of the experimental setup. (c) Local linear model fits to the fractional occupancy for filter width h = 270 s. (d) Calculated concentration. The symbols and error bars represent the calculated mode of the concentration distribution divided by K_D over a 5% to 95% confidence interval.

binding time, $1/k_d$ = 1000 s, which results in delayed sensitivity to sudden decreases in concentration. Increasing h improves the signal to noise ratio of the calculated concentration at the expense of time resolution (see Supplementary Data).

3.3. Calibration of plasmonic nanostructures

Our experiments take place on an inverted wide-field microscope using glass coverslips that have been patterned via electron beam lithography to incorporate arrays of plasmonic gold nanostructures (Fig. 1a). The structures, 75 nm in diameter and 80 nm in height, were arranged in 20 × 20 arrays with a pitch of either 300 nm or 500 nm between nanostructures and 33 μm between arrays, center-to-center. They are illuminated with a 100 W halogen lamp and crossed polarizers are used to minimize background contributions from glass substrate scattered light. In aqueous solutions the arrays have a resonance peak centered at ~635 nm. The gold nanostructures are biologically functionalized by first applying a two-component self-assembled monolayer of thiols in a 3:1 ratio. The majority

http://dx.doi.org/10.1016/j.heliyon.2017.e00340

thiol component is terminated with polyethylene glycol to prevent non-specific binding while the slightly longer minority component terminates with an amine group for covalent ligand attachment. Analyte binding to the ligands causes a perturbation in the local index of refraction which is manifested as a spectral red shift and increase in intensity (Fig. 1b inset). When imaged, the arrays are observed to brighten with increasing spectral shift.

Our configuration integrates with traditional cell microscopy techniques such as fluorescence and brightfield imaging, which are accessible by the automated switching of a filter cube (Raphael et al., 2013a). In order to infer secreted protein concentration from imagery, the qualitative feature of array brightening on the CCD camera must be quantified in terms of the fractional occupancy, f. To accomplish this calibration we used the setup shown in Fig. 1a in which spectroscopy and imagery are recorded simultaneously for a given array while the analyte is microfluidically introduced. We have previously shown that f can be determined from spectroscopy data by tracking the spectral shift as the analyte concentration is increased from zero to a saturating value (Raphael et al., 2012; Raphael et al., 2013b). Fig. 1b shows an application of this spectrometry-based technique in which fractional occupancy was determined from the introduction of 400 nM of anti-c-myc monoclonal antibodies over c-myc peptide functionalized nanostructures. However, the information gained from binning by wavelength in spectroscopy-based approaches comes at the expense of spatio-temporal resolution. For instance, in the optical configuration of Fig. 1a, the spectral spatio-temporal resolutions were over an order of magnitude lower than those of the CCD camera. To determine the fractional occupancy directly from imagery (LSPRi), the mean array intensity as measured by the camera, $I(t)$, was normalized by $I_N(t) = (I(t) - I_o)/(I_f - I_o)$ where I_o and I_f are the initial and saturated array intensity values (Fig. 1c). When plotted against the spectrally-determined fractional occupancy (Fig. 1d) a linear relationship is evident. This relationship holds whether the analyte is a 150 kDa antibody such as anti-c-myc (red and green data) or 60 kDa neutravidin proteins binding to a biotinylated surface (blue data). As a result of this design and calibration, every array in the LSPRi field of view could be used to determine fractional occupancy in real time, without the need for spectrometry.

3.4. Live cell secretion measurements

Antibody producing hybridoma cells are utilized for both diagnostics and therapeutics (Galluzzi et al., 2012; Gavilondo and Larrick, 2000), making their secretion rate characterization of critical importance. In this application, anti-c-myc secreting hybridoma cells were introduced on to a chip with c-myc functionalized nanostructures. The density of cells was adjusted so that the field of view included 2 to 3 cells. At a distance of 70 μm or more from the cells, the secreted antibody

http://dx.doi.org/10.1016/j.heliyon.2017.e00340

concentration fell below the array detection limit (~100 pM) allowing for those arrays to be used as negative controls. By having controls in the same field of view, global intensity variations such as those due to focus drift could be subtracted out from the signal of arrays adjacent to cells. At the end of each experiment, a saturating solution of commercial anti-c-myc antibodies was introduced in order to normalize the LSPRi intensity and calculate fractional occupancy as described above. The excitation wavelengths used in nanoplasmonic imaging (625 nm−700 nm) scatter weakly from live cells enabling measurements to be made when the distance from cell surface to array center was 3 μm or greater. Measurements were still possible in cases which cells were within a few microns of the arrays but the signal to noise is typically diminished. In such cases, light scattering from the cell presented a distinct stochastic signature due to membrane fluctuations which were readily identified in the array data by the increased noise in the image intensity (Raphael et al., 2013a). Because the same noise is not observed in arrays farther from the cell, its source is clear. The kinetic rate constants used in the analysis were determined with a commercial SPR instrument using an identical surface functionalization protocol to that of the nanoplasmonic substrates (Raphael et al., 2013b) $k_a = 2.68 \times 10^4\ \mathrm{M^{-1}s^{-1}}$, $k_d = 4.75 \times 10^{-5}\ \mathrm{s^{-1}}$ and $K_D = k_d/k_a =$ 1.77 nM.

The simultaneous secretion measurements from two cells are shown in Fig. 4. Arrays adjacent to the cells used for the analysis are marked with red and blue boxes; the white box outlines the control array. The time dependent fractional occupancy (Fig. 4b) indicates that the lower cell was secreting at a higher rate than the upper cell. Concentration, determined using a temporal filter with h = 270 s, was constant over 40 min as expected for a steady state secretion scenario, with an average concentration of 1.30 nM near the lower cell versus 230 pM for the upper cell. For clarity, only the data from the arrays closest to the cells are displayed which span the range of fractional occupancies measured. Data from other arrays are shown in the Supplementary Data, Fig. S4. Given that the signals measured in Fig. 4 were near the limit of detection, we cannot rule out the possibility that small pulses or stops and starts to the secretion process were also occuring.

In contrast to Fig. 4, the collection of three cells shown in Fig. 5a displayed strongly time dependent secretions. The array to the left of the cells (green outline) measured a rise in fractional occupancy (Fig. 5b) that rose to 0.28 over the course of 2 min. This is in sharp contrast from the cells of Fig. 4 in which it took 40 min to reach a maximum fractional occupancy of 0.08. The concentration for the green-outlined array, located 24 μm from the center of the three cells, peaked at 56 nM within 2 min (Fig. 5c). The rapid increase and decrease in concentration was best resolved using a temporal filter with h = 45 s. The burst was also recorded by the red-outlined array located 43 μm from the center of the three cells. The peak concentration at this array was 9 nM and time-delayed by 91 s from the green-

http://dx.doi.org/10.1016/j.heliyon.2017.e00340

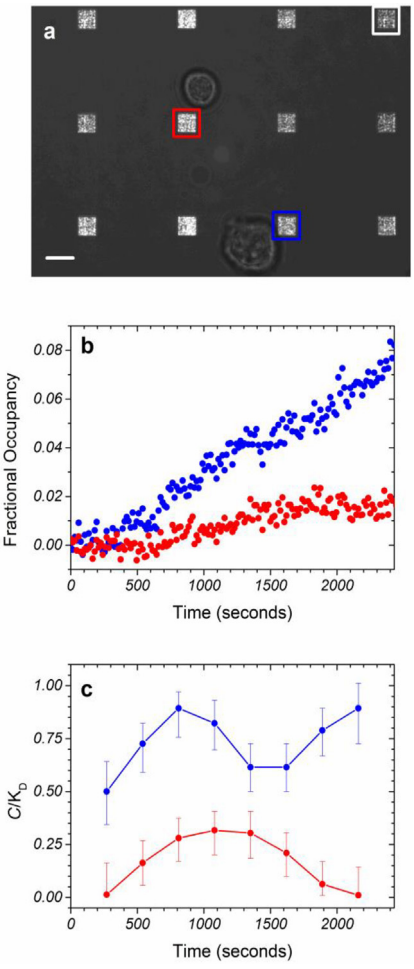

Fig. 4. Steady state secretions quantified. (a) Merged LSPRi and brightfield images showing two hybridoma cells amongst 12 arrays. The arrays outlined in red and blue were used to measure the antibody concentration near the upper and lower cells, respectively, while the array outlined in white was used as a control. (b) LSPRi-determined fractional occupancy. Red and blue data points correspond to red and blue outlined arrays from (a) after subtracting control array data. (c) Calculated concentration for the red and blue outlined arrays applying a temporal filter with h = 270 s. The symbols and error bars represent the mode of the concentration probability distribution divided by K_D with a 5% to 95% confidence interval. Time t = 0 s was defined to be approximately 500 s before the signal rose above the noise. Scale bar is 8 μm.

outlined array peak, consistent with a burst of secreted antibodies diffusing outwardly from the three cells. It was unclear from the imagery how many of the cells contributed to the burst. For clarity, arrays have been selected for analysis that span the range of fractional occupancies measured. Data from other arrays are shown in the Supplementary Data, Fig. S5.

http://dx.doi.org/10.1016/j.heliyon.2017.e00340

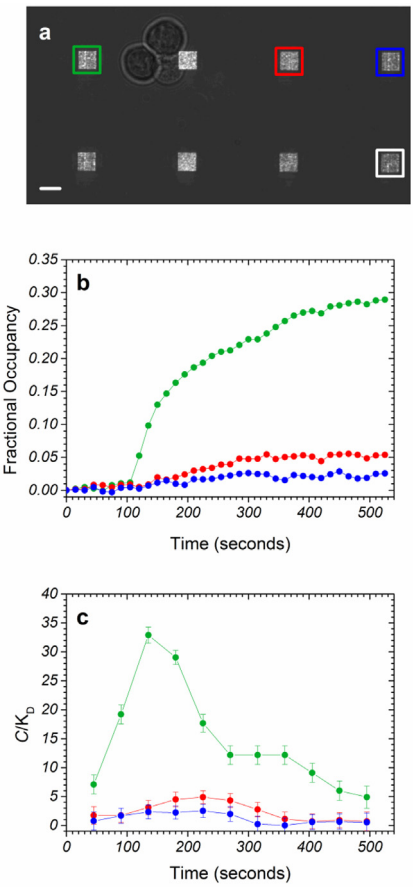

Fig. 5. Burst secretion quantified. (a) Merged LSPRi and brightfield images showing a cluster of three hybridoma cells amongst 8 arrays. The arrays outlined in green, red and blue were used to measure the concentration at varying distances from the cell while the array outlined in white was used as a control. (b) LSPRi-determined fractional occupancy. Green, red and blue data points correspond to the green, red and blue outlined arrays in (a) after subtracting the control array data. (c) Calculated concentration for the green, red and blue outlined arrays applying temporal filter analysis with h = 45 s. The symbols and error bars represent the calculated mode of the concentration probability distribution divided by K_D at each time point with a 5% to 95% confidence interval. Time t = 0 s was defined to be approximately 100 s before the signal rose above the noise. The scale bar is 8 μm.

A comparison of the *h* values used in Fig. 4c and Fig. 5c highlights the importance of taking an adaptive approach to the data analysis. The Fig. 4 data, being steady state in nature, can accommodate the longer *h* value (270 s) without loss of temporal information and take advantage of the improved signal-to-noise (Supplementary Data). In Fig. 5c, the signal-to-noise is reduced by the shorter *h* value but the peaks in time are readily resolved. The dynamic range of the sensors is also highlighted by these two figures in which the 56 nM peak of Fig. 5 is 244-fold greater than the concentration measured at the lower cell of Fig. 4a. In general, the optimally designed sensor will have a K_D value centered within the range of possible secreted concentrations. Finally, the fact that multiple arrays at varying

http://dx.doi.org/10.1016/j.heliyon.2017.e00340

distances from the cell in Fig. 5 could be utilized to measure the burst secretion underscores the spatial and temporal capabilities of our approach.

4. Conclusions

The results presented here demonstrate that local linear models can be applied to infer time-varying analyte concentrations in solution as secreted by 9E10 hybridoma cells. An adjustable time window filter is incorporated into the models to allow for data that can range from smoothly varying to discrete jumps. Our hope is that by basing the analysis on time-dependent fractional occupancy measurements this approach can be applied to other experimental techniques (*i.e.* immunosandwich assays) which also measure this variable.

The experimental approach was aided by the fact that healthy hybridoma cells can secrete their antibodies at a rate of 1000 antibodies/s, swamping all other supernatant proteins. This significantly reduced the competition from non-specific binding and simplified our analysis. Future applications of nanoplasmonic imaging to slower secreting cell lines will likely require a wash step to remove non-specifically bound proteins from the sensor surface.

Declarations

Author contribution statement

Jeff M. Byers: Analyzed and interpreted the data; Contributed reagents, materials, analysis tools or data; Wrote the paper.

Joseph A. Christodoulides, James B. Delehanty: Contributed reagents, materials, analysis tools or data.

Deepa Raghu: Performed the experiments.

Marc Raphael: Conceived and designed the experiments; Performed the experiments; Analyzed and interpreted the data; Wrote the paper.

Funding statement

This work was supported by the Naval Research Laboratory's Institute for Nanoscience, the Office of the Assistant Secretary of Defense for Research & Engineering (Vannevar Bush Award) and a National Research Council Research Postdoc Associateship Award.

Competing interest statement

The authors declare no conflict of interest.

http://dx.doi.org/10.1016/j.heliyon.2017.e00340

Additional information

Supplementary content related to this article has been published online at http://dx.doi.org/10.1016/j.heliyon.2017.e00340.

See Supplementary Data for details of the concentration calculation derivation, discussion of choosing an optimal model filter width and additional array data analysis.

References

Ashkenazi, A., Dixit, V.M., 1998. Death receptors: Signaling and modulation. Science 281, 1305–1308.

Beck, L., Damore, P.A., 1997. Vascular development: Cellular and molecular regulation. FASEB J. 11, 365–373.

Brandley, B.K., Schnaar, R.L., 1989. Tumor-cell haptotaxis on covalently immobilized linear and exponential gradients of a cell-adhesion peptide. Dev. Biol. 135, 74–86.

Conlon, I.J., Dunn, G.A., Mudge, A.W., Raff, M.C., 2001. Extracellular control of cell size. Nat. Cell Biol. 3, 918–921.

Dertinger, S.K.W., Jiang, X.Y., Li, Z.Y., Murthy, V.N., Whitesides, G.M., 2002. Gradients of substrate-bound laminin orient axonal specification of neurons. Proc. Natl. Acad. Sci. USA 99, 12542–12547.

El-Ali, J., Sorger, P.K., Jensen, K.F., 2006. Cells on chips. Nature 442, 403–411.

Friedl, P., Gilmour, D., 2009. Collective cell migration in morphogenesis, regeneration and cancer. Nat. Rev. Mol. Cell Biol. 10, 445–457.

Galluzzi, L., Vacchelli, E., Fridman, W.H., Galon, J., Sautes-Fridman, C., Tartour, E., Zucman-Rossi, J., Zitvogel, L., Kroemer, G., 2012. Trial watch Monoclonal antibodies in cancer therapy. Oncoimmunology 1, 28–37.

Gavilondo, J.V., Larrick, J.W., 2000. Antibody engineering at the millennium. Biotechniques 29, 128–132.

Han, Q., Bradshaw, E.M., Nilsson, B., Hafler, D.A., Love, J.C., 2010. Multidimensional analysis of the frequencies and rates of cytokine secretion from single cells by quantitative microengraving. Lab Chip 10, 1391–1400.

Heldin, C.H., Westermark, B., 1999. Mechanism of action and in vivo role of platelet-derived growth factor. Physiol. Rev. 79, 1283–1316.

Hershko, A., Ciechanover, A., 1998. The ubiquitin system. Annu. Rev. Biochem. 67, 425–479.

Hogan, B.L.M., 1996. Bone morphogenetic proteins: Multifunctional regulators of vertebrate development. Genes Dev. 10, 1580–1594.

Jeon, N.L., Baskaran, H., Dertinger, S.K.W., Whitesides, G.M., Van de Water, L., Toner, M., 2002. Neutrophil chemotaxis in linear and complex gradients of interleukin-8 formed in a microfabricated device. Nature Biotechnol. 20, 826–830.

Letterio, J.J., Roberts, A.B., 1998. Regulation of immune responses by TGF-beta. Annu. Rev. Immunol. 16, 137–161.

Licko, V., 1973. Threshold secretory mechanism-model of derivative element in biological control. Bull. Math. Biol. 35, 51–58.

Lucchetta, E.M., Lee, J.H., Fu, L.A., Patel, N.H., Ismagilov, R.F., 2005. Dynamics of Drosophila embryonic patterning network perturbed in space and time using microfluidics. Nature 434, 1134–1138.

Nagata, S., 1997. Apoptosis by death factor. Cell 88, 355–365.

Raff, M.C., Abney, E., Brockes, J.P., Hornbysmith, A., 1978. Schwann cell growth factors. Cell 15, 813–822.

Raphael, M.P., Christodoulides, J.A., Delehanty, J.B., Long, J.P., Byers, J.M., 2013a. Quantitative Imaging of Protein Secretions from Single Cells in Real Time. Biophys. J. 105, 602–608.

Raphael, M.P., Christodoulides, J.A., Mulvaney, S.P., Miller, M.M., Long, J.P., Byers, J.M., 2012. A new methodology for quantitative LSPR biosensing and imaging. Anal. Chem. 84, 1367–1373.

Raphael, M.P., Christodoulides, J.A., Delehanty, J.B., Long, J.P., Pehrsson, P.E., Byers, J.M., 2013b. Quantitative LSPR imaging for biosensing with single nanostructure resolution. Biophys. J. 104, 30–36.

Risau, W., Flamme, I., 1995. Vasculogenesis. Annu. Rev. Cell Dev. Biol. 11, 73–91.

Shirasaki, Y., Yamagishi, M., Suzuki, N., Izawa, K., Nakahara, A., Mizuno, J., Shoji, S., Heike, T., Harada, Y., Nishikomori, R., Ohara, O., 2014. Real-time single-cell imaging of protein secretion. Sci. Rep. 4.

Sunnaker, M., Zamora-Sillero, E., Dechant, R., Ludwig, C., Busetto, A.G., Wagner, A., Stelling, J., 2013. Automatic Generation of Predictive Dynamic Models Reveals Nuclear Phosphorylation as the Key Msn2 Control Mechanism. Sci. Signal. 6.

Tsaneva-Atanasova, K., Osinga, H.M., Tabak, J., Pedersen, M.G., 2010. Modeling Mechanisms of Cell Secretion. Acta Biotheor. 58, 315–327.

 http://dx.doi.org/10.1016/j.heliyon.2017.e00340

Werner, S., Grose, R., 2003. Regulation of wound healing by growth factors and cytokines. Physiol. Rev. 83, 835–870.

Whitesides, G.M., Ostuni, E., Takayama, S., Jiang, X.Y., Ingber, D.E., 2001. Soft lithography in biology and biochemistry. Annu. Rev. Biomed. Eng. 3, 335–373.

Yang, M.S., Li, C.W., Yang, J., 2002. Cell docking and on-chip monitoring of cellular reactions with a controlled concentration gradient on a microfluidic device. Anal. Chem. 74, 3991–4001.

 http://dx.doi.org/10.1016/j.heliyon.2017.e00340